Available online at www.sciencedirect.com
SCIENCE DIRECT®
PERGAMON
International Journal of Heat and Mass Transfer 46 (2003) 2819–2832
International Journal of HEAT and MASS TRANSFER
www.elsevier.com/locate/ijhmt

Influence of convection and grain movement on globular equiaxed solidification

Menghuai Wu *, Andreas Ludwig, Andreas Bührig-Polaczek, Martin Fehlbier, Peter R. Sahm

Foundry Institute, Aachen University (RWTH), Intzestr. 5, D-52072 Aachen, Germany

Received 20 March 2002; received in revised form 8 January 2003

Abstract

A two-phase volume averaging model was used to study convection and grain movement, and their influence on the globular equiaxed solidification. Both liquid and solid phases were treated as separate interpenetrating continua. The mass, momentum, species and enthalpy conservation equations for each phase and a grain transport equation were coupled. An ingot casting (Al–4 wt.% Cu) with near globular solidification morphology was simulated. Case studies with different modeling assumptions such as with and without grain movement, and with slip and non-slip boundary conditions for solid phase were presented and compared. Understanding of grain evolution and macrosegregation formation in globular equiaxed solidification was improved.

Keywords: Convection; Grain movement; Modeling; Solidification; Two-phase; Ingot casting; Macrosegregation; Grain evolution

1. Introduction

Melt convection and grain movement play an important role in the solidification of metal castings. Different macrosegregation patterns are formed or at least strongly influenced by the melt flow and grain movement [1–3]. Numerical methods to study these phenomena have only been developed in recent years, when all the conservation equations (mass, momentum, energy, solute, even the grain transport) were able to be coupled and solved simultaneously.

One numerical approach was based on a 'mixture' theory [4–11] with the two-phase problem (liquid and solid) as a single phase, a pseudo-fluid. The transport equations, which were supposed to be equally valid in bulk melt, mushy zone and solid regions by assigning respective 'physical properties', were solved with a single-domain numerical method on a fixed grid system. The obvious drawback of this 'mixture' model is that it fails to describe the interaction between the liquid and solid phases, and the thermal and constitutional non-equilibrium at the liquid–solid interface. An other approach is to use a multiphase model such as the one developed by Beckermann's group [12–18] which is based on the volume averaging theorem. They treated the liquid and solid as separate interpenetrating continua, established and solved the transport equations (mass, momentum, energy and solute) for the liquid and solid simultaneously, thereby permitting a rigorous description of disparate solid and liquid velocities, interactions, thermal and constitutional non-equilibrium, and many other microscopic phenomena. With a two-phase volume averaging approach the authors [19–21] focus on globular equiaxed solidification, and some parameters used in the Backermann's model [7,8,12] to describe the dendritic solidification morphology were avoided. Further study to understand and describe the dendritic morphology is actually necessary [22].

In this paper the two-phase globular equiaxed solidification model was used to study melt convection and grain movement phenomena in solidification. Both the nucleation law and the growth kinetics [23–25] were implemented in the macro transport equations. An Al–4

* Corresponding author. Tel.: +49-0241-8094067; fax: +49-0241-8092276.
E-mail address: menghuai@gi.rwth-aachen.de (M. Wu).

0017-9310/03/$ - see front matter
doi:10.1016/S0017-9310(03)00054-1

Nomenclature

c_0 initial concentration
c_l, c_s species concentration
c^* interface species concentration
$C_{ls} (= -C_{sl})$ species exchange rate, kg m^{-3} s^{-1}
$C^d_{ls} (= -C^d_{sl})$ species diffusional flux, kg m^{-3} s^{-1}
$C^p_{ls} (= -C^p_{sl})$ species exchange due to phase change, kg m^{-3} s^{-1}
c_{mix} mixture concentration
$c_{p(l)}, c_{p(s)}$ specific heat, J kg^{-1} K^{-1}
D_l, D_s diffusion coefficient, m^2 s^{-1}
d_s grain diameter, μm (10^{-6} m)
f_l, f_s volume fraction
f^c_s grain packing limit
$\vec{g}$ gravity, m s^{-2}
g_α growth factor, m s^{-1}
H heat transfer coefficient at metal/mold interface, W m^{-2} K^{-1}
H^* volume heat exchange rate between solid and liquid phases, W m^{-3} K^{-1}
h_l, h_s enthalpy, J kg^{-1}
h^* interface enthalpy, J kg^{-1}
Δh_f latent heat (heat of fusion), J kg^{-1}
$K_{sl} (= K_{ls})$ momentum exchange coefficient, kg m^{-3} s^{-1}
k partitioning coefficient of phase diagram
k_l, k_s thermal conductivity, W m^{-1} K^{-1}
$M_{ls} (= -M_{sl})$ mass transfer rate, kg s^{-1} m^{-3}
m slope of liquidus in phase diagram, K
N grain production rate, m^{-3} s^{-1}
n grain density, m^{-3}
n_{max} maximum grain density, m^{-3}
p pressure, Pa
p_0 initial pressure, Pa
$Q_{ls} (= -Q_{sl})$ energy exchange rate, J m^{-3} s^{-1}
$Q^d_{ls} (= -Q^d_{sl})$ energy exchange by heat transfer, J m^{-3} s^{-1}
$Q^p_{ls} (= -Q^p_{sl})$ energy change due to phase change, J m^{-3} s^{-1}
T_0 initial temperature, K
T, T_l, T_s temperature, K
T_E eutectic temperature, K
T_f melting point of pure metal (Al), K
T_{w1} boundary temperature, K
T_{ref} reference temperature for enthalpy definition, K
ΔT undercooling, K
ΔT_N mean nucleation undercooling corresponding to maximum nucleation rate, K
ΔT_σ standard deviation of the Gaussian distribution, K
t time, s
$\vec{U}_{ls} (= -\vec{U}_{sl})$ momentum exchange rate, kg m^{-2} s^{-2}
$\vec{U}^d_{ls} (= -\vec{U}^d_{sl})$ momentum change due to drag force, kg m^{-2} s^{-2}
$\vec{U}^p_{ls} (= -\vec{U}^p_{sl})$ momentum exchange due to phase change, kg m^{-2} s^{-2}
u_l, u_s velocity component in x-direction, m s^{-1}
$\vec{u}_l, \vec{u}_s$ velocity vector, m s^{-1}
$\vec{u}_{ls}, \vec{u}_{sl}$ interphase velocity, m s^{-1}
$\vec{u}^\infty_l$ free stream velocity, m s^{-1}
$\vec{u}^*$ interface velocity, m s^{-1}
v_l, v_s velocity component in y-direction, m s^{-1}
$\tilde{y}$ distance along the wall from the starting point of the boundary layer, m
$\Delta\delta$ distance from the adjacent wall cell center to the wall, m
ρ_l, ρ_s density, kg m^{-3}
μ_l, μ_s viscosity, kg m^{-1} s^{-1}
μ_{mix} viscosity of the solid–liquid mixture, kg m^{-1} s^{-1}
$\bar{\bar{\tau}}_l, \bar{\bar{\tau}}_s$ stress–strain tensors, kg m^{-1} s^{-2}

Subscripts
l, s mark liquid and solid phases

wt.% Cu ingot casting was simulated. With a ppm of Ti as the grain finer this alloy solidifies with a near globular equiaxed rather than a distinct dendritic morphology. Emphases were placed on the melt convection and grain movement, and their influence on solidification sequence, grain evolution and macrosegregation formation.

2. Modeling and numerical procedure

The two-phase volume averaging model for globular equiaxed solidification [19–21] was described previously, and therefore, only a short description is presented here. The conservation equations, source terms, exchange terms and some auxiliary terms are shown in Table 1. Derivation of the equations and description of the volume averaging theorem are detailed in literature [12,19].

2.1. Conservation equations

The liquid and solid phases are transported according to the mass conservation in the momentum equation (1), taking solidification (or remelting) into account through a mass transfer term $M_{ls} (= -M_{sl})$, which is

Table 1
Conservation equations, source and exchange terms and auxiliary equations for the numerical model of globular equiaxed solidification

Conservation equations

Mass:

$$\frac{\partial}{\partial t}(f_l\rho_l) + \nabla\cdot(f_l\rho_l\vec{u}_l) = M_{sl}$$
$$\frac{\partial}{\partial t}(f_s\rho_s) + \nabla\cdot(f_s\rho_s\vec{u}_s) = M_{ls} \quad (1)$$

Momentum:

$$\frac{\partial}{\partial t}(f_l\rho_l\vec{u}_l) + \nabla\cdot(f_l\rho_l\vec{u}_l\otimes\vec{u}_l) = -f_l\nabla p + \nabla\cdot\bar{\bar{\tau}}_l + f_l\rho_l\vec{g} + \vec{U}_{sl}$$
$$\frac{\partial}{\partial t}(f_s\rho_s\vec{u}_s) + \nabla\cdot(f_s\rho_s\vec{u}_s\otimes\vec{u}_s) = -f_s\nabla p + \nabla\cdot\bar{\bar{\tau}}_s + f_s\rho_s\vec{g} + \vec{U}_{ls} \quad (2)$$

where $\bar{\bar{\tau}}_l = \mu_l f_l(\nabla\cdot\vec{u}_l + (\nabla\cdot\vec{u}_l)^T)$ and $\bar{\bar{\tau}}_s = \mu_s f_s(\nabla\cdot\vec{u}_s + (\nabla\cdot\vec{u}_s)^T)$

Species:

$$\frac{\partial}{\partial t}(f_l\rho_l c_l) + \nabla\cdot(f_l\rho_l\vec{u}_l c_l) = \nabla\cdot(f_l\rho_l D_l\nabla c_l) + C_{sl}$$
$$\frac{\partial}{\partial t}(f_s\rho_s c_s) + \nabla\cdot(f_s\rho_s\vec{u}_s c_s) = \nabla\cdot(f_s\rho_s D_s\nabla c_s) + C_{ls} \quad (3)$$

Enthalpy:

$$\frac{\partial}{\partial t}(f_l\rho_l h_l) + \nabla\cdot(f_l\rho_l\vec{u}_l h_l) = \nabla\cdot(f_l k_l\nabla\cdot T_l) + Q_{sl}$$
$$\frac{\partial}{\partial t}(f_s\rho_s h_s) + \nabla\cdot(f_s\rho_s\vec{u}_s h_s) = \nabla\cdot(f_l k_s\nabla\cdot T_s) + Q_{ls} \quad (4)$$

where $h_l = \int_{T_{ref}}^{T_l} c_{p(l)}\,dT + h_l^{ref}$ and $h_s = \int_{T_{ref}}^{T_s} c_{p(s)}\,dT + h_s^{ref}$

Grain:

$$\frac{\partial}{\partial t}n + \nabla\cdot(\vec{u}_s n) = N \quad (5)$$

Source terms

Nucleation:

$$N = \frac{d\Delta T}{dt}\frac{n_{max}}{\sqrt{2\pi}\cdot\Delta T_\sigma}\exp\left(-\frac{1}{2}\left(\frac{\Delta T - \Delta T_N}{\Delta T_\sigma}\right)^2\right) \quad (6)$$

Exchange terms

Mass:

$$M_{ls} = g_\alpha\cdot\Delta c\cdot(n\cdot\pi d_s^2)\cdot\rho_s\cdot f_l \quad (7)$$

Momentum:

$$\vec{U}_{ls} = \vec{U}_{ls}^d + \vec{U}_{ls}^p \quad \vec{U}_{ls}^p = \vec{u}^*\cdot M_{ls} \quad \vec{U}_{ls}^d = K_{ls}(\vec{u}_l - \vec{u}_s) \quad (8)$$

Species:

$$C_{ls} = C_{ls}^d + C_{ls}^p \quad C_{ls}^p = c^*\cdot M_{ls} \quad C_{ls}^d \text{ neglected} \quad (9)$$

Enthalpy:

$$Q_{ls} = Q_{ls}^d + Q_{ls}^p \quad Q_{ls}^p = h^*\cdot M_{ls} \quad Q_{ls}^d = H^*\cdot(T_l - T_s) \quad (10)$$

Auxiliary terms

Mixture concentration:

$$c_{mix} = \frac{c_l\cdot\rho_l\cdot f_l + c_s\cdot\rho_s\cdot f_s}{\rho_l\cdot f_l + \rho_s\cdot f_s} \quad (11)$$

Grain diameter:

$$d_s = (6f_s/\pi\cdot n)^{\frac{1}{3}} \quad (12)$$

Solid viscosity:

$$\mu_s = \begin{cases}\dfrac{\mu_l}{f_s}\cdot\left((1-f_s/f_s^c)^{-2.5f_s^c} - (1-f_s)\right) & \text{when } f_s < f_s^c \\ \infty & \text{else}\end{cases} \quad (13)$$

defined in Eq. (7). Details of M_{ls} are given in Section 2.3. The volume fractions of both phases are subject to $f_l + f_s = 1$.

A 'viscosity' of the solid μ_s in the momentum conservation equation (2) is employed. It is empirically defined in Eq. (13) based on the mixing rule: [13–16] $\mu_{mix} = f_l\mu_l + f_s\mu_l$. μ_s is the same order of μ_l when the f_s is small. As the f_s approaches the packing limit f_s^c, which is taken as 0.637 for globular grains, μ_s increases infinitely. Therefore beyond the packing limit, the solid becomes rigid. However, the melt penetrates the voids of the closely packed grains.

Momentum exchange $\vec{U}_{ls}$ $(=-\vec{U}_{sl})$ consists of two parts: one due to mass transfer $\vec{U}^{p}_{ls}$ and the other due to friction and drag $\vec{U}^{d}_{ls}$. Both terms are given in Eq. (8). In order to define $\vec{U}^{p}_{ls}$, two different situations must be considered: solidification and remelting. For solidification, the momentum transferred from liquid to solid is determined by the velocity of the melt $\vec{u}_l$ and the mass transfer rate M_{ls}, hence $\vec{U}^{p}_{ls} = \vec{u}^{*} \cdot M_{ls}$ with $\vec{u}^{*} = \vec{u}_l$. By analogy we have $\vec{U}^{p}_{ls} = \vec{u}^{*} \cdot M_{ls}$ with $\vec{u}^{*} = \vec{u}_s$ for remelting. In the friction and drag term $\vec{U}^{d}_{ls}$, there are two situations: below and beyond the packing limit f^{c}_{s}. For the low fraction solid ($f_s < f^{c}_{s}$), the solidified grains behave analogously to submerging objects, and therefore we used the Kozeny–Carman [26] model. Beyond the packing limit ($f_s \geqslant f^{c}_{s}$), we employed the porous medium model by Blake–Kozeny [26]. Details about these models are given elsewhere [19,26,27].

The average solute concentrations in the melt c_l and in the solid c_s are obtained from the species conservation equation (3). The solute exchange C_{ls} $(=-C_{sl})$ between solid and liquid includes two parts: solute partitioning at the liquid–solid interface due to phase change C^{p}_{ls} and solute diffusional exchange at the interface C^{d}_{ls}. Here the diffusional term C^{d}_{ls} is negligible. For the partitioning term C^{p}_{ls}, two situations are considered: solidification and remelting. During solidification the solute mass transfer rate from the liquid to the solid without solute partitioning is $c_l \cdot M_{ls}$. Due to partitioning, however, the solid can only accept $k \cdot c_l \cdot M_{ls}$. The rest of solute $(1-k) \cdot c_l \cdot M_{ls}$ remains in the liquid, enriching solute in the melt. Therefore, we have $C^{p}_{ls} = c^{*} \cdot M_{ls}$ with $c^{*} = k \cdot c_l$ for solidification in Eq. (9). During remelting the solute mass transfer rate from solid to liquid is $c_s \cdot M_{sl}$. The solute mass is now completely accepted by the liquid. Therefore, we have $C^{p}_{sl} = c^{*} \cdot M_{sl}$ with $c^{*} = c_s$ for remelting in Eq. (9). Additionally, in order to predict the macrosegregation a mixture concentration is calculated with Eq. (11).

The energy conservation equations (4) for both phases are solved separately. The exchange term Q_{ls} $(=-Q_{sl})$ is defined in Eq. (10). Two parts are included in the Q_{ls}: one due to phase change Q^{p}_{ls} and the other due to the liquid–solid interface heat transfer Q^{d}_{ls}. Our model assumes thermal equilibrium, i.e. $T_l = T_s$. To ensure this equilibrium, a very large heat transfer coefficient ($H^{*} = 10^{9}$ W/m^3/K) between the liquid and the solid is applied. To handle the term Q^{p}_{ls}, solidification and remelting are also considered separately. During solidification the enthalpy per unit volume and time which should be transferred from the liquid to the solid is $h_l \cdot M_{ls}$. Referring to Eq. (10) we thus have $Q^{p}_{ls} = h^{*} \cdot M_{ls}$ with $h^{*} = h_l$. At the same temperature the liquid enthalpy h_l is higher than the solid enthalpy h_s. The enthalpy difference ($h_l - h_s = \Delta h_f$) defines the latent heat. The transfer of Q^{p}_{ls} does not change the h_l directly, but forces h_s to increase, hence cause the solid temperature to rise locally. With the precondition of thermal equilibrium ($T_l = T_s$), the temperatures of the liquid and solid are balanced through volume heat exchange rate (H^{*}) between the phases. In this study, test simulations were carried out, and a suitably large value for H^{*} (10^{9} W m^{-2} K^{-1}) is obtained. With this parameter the precondition of thermal equilibrium is maintained and the numerical calculation results are stable. By analogy we have $Q^{p}_{sl} = h^{*} \cdot M_{sl}$ with $h^{*} = h_s$ for melting.

Grain conservation is formulated in Eq. (5). The grain density n is transported according to the solid velocity. The source term N, namely the grain production rate, is defined in Eq. (6), and described in the following section.

2.2. Nucleation and grain transport

To describe the nucleation event in the presence of melt convection and grain movement the pragmatic approach originally developed by Oldfield [28] was used. This approach is based on the assumption that many potential nucleation sites exist in the parent melt, e.g. the inoculant particles through grain refiner. The nucleation sites belong to different families. Each family can only be activated as newly nucleated grains when a corresponding undercooling ΔT is achieved. ΔT is defined as $T_f + m \cdot c_l - T$ (Fig. 1). The undercooling ΔT serves as the only driving force for nucleation. A Gaussian distribution describes the statistical outcome of all the families of the nucleation sites (Fig. 2),

$$\frac{\mathrm{d}n}{\mathrm{d}\Delta T} = \frac{n_{\max}}{\sqrt{2\pi} \cdot \Delta T_{\sigma}} \exp\left(-\frac{1}{2} \left(\frac{\Delta T - \Delta T_N}{\Delta T_{\sigma}} \right)^{2} \right) \tag{14}$$

ΔT_N is the mean nucleation undercooling corresponding to the maximum of the distribution, ΔT_{σ} is the standard deviation of the distribution, $n_{\max}$ is the maximum density of nuclei given by the integral of the total distribution from zero undercooling to infinite undercooling. According to Rappaz [23], these three parameters can be determined experimentally for each melt by measuring the grain density (i.e. the grain size) and the corresponding maximum undercooling at recalescence, $\Delta T_{\max}$.

In the numerical model the potential nucleation sites are assumed to be stationary. Only the nucleated grains move according to Eq. (5). Taking a volume element as an example, the potential nucleation sites in it are previously assigned. As an undercooling ΔT is achieved, a certain amount of grains corresponding to this undercooling ΔT are nucleated. The sites from which the grains have already nucleated are exhausted from the

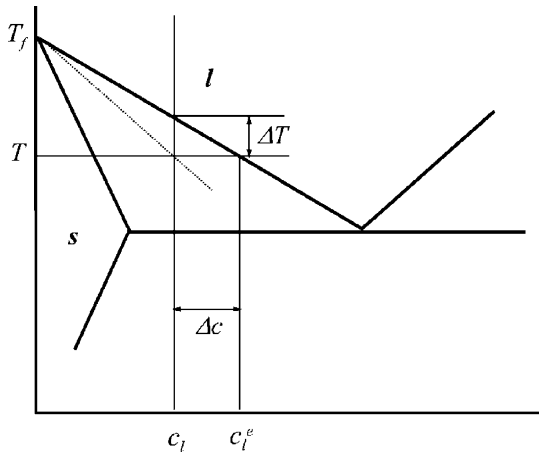

Fig. 1. Phase diagram of a binary system. The driving force for nucleation is defined by the constitutional undercooling.

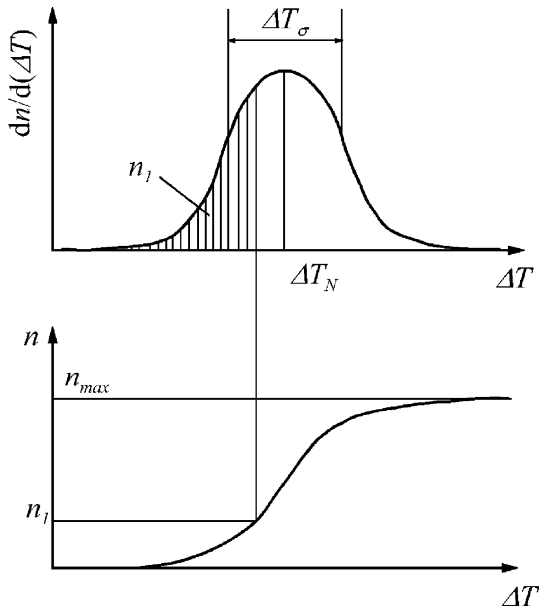

Fig. 2. A heterogeneous nucleation law. At a given undercooling, the grain density is given by integral of the distribution.

control volume element. The remaining nucleation sites can only be activated by greater undercooling. The maximum ΔT ever achieved for the considered volume element is recorded as $\Delta T_{\max}$. As time proceeds, the actual ΔT is much smaller than $\Delta T_{\max}$. Thus there is no further nucleation. When the actual ΔT is larger than $\Delta T_{\max}$, new grains nucleate, and we further reset $\Delta T_{\max}$ as the actual ΔT, and so on. Whether nucleated grains remain in this volume element, or move to the neighboring elements, does not influence the above nucleation procedure. In the case of remelting (grains are exposed to the overheated melt), the nucleation rate is set to zero until the fraction solid drops below 0.01%. Then a negative nucleation rate is calculated similar to the above description as the grain dissolution rate.

In order to apply the nucleation law in the numerical model, N in Eq. (5) is defined as

$$\frac{\mathrm{d}n}{\mathrm{d}(\Delta T)}\frac{\mathrm{d}(\Delta T)}{\mathrm{d}t}$$

Because nucleation can occur in a partially solidified volume element, an Avrami-factor f_l is additionally considered in Eq. (6).

2.3. Grain growth and mass transfer

As grains nucleate they start to grow. The Ti-inoculated Al–4 wt.% Cu alloy solidifies with a near globular equiaxed rather than a distinct dendritic morphology. The average diameter d_s of the grains can be determined from the fraction solid f_s and the grain density n according to Eq. (12).

As the grain grows, the solute element piles up ($k < 1$) in front of the liquid–solid interface due to solute partitioning. The enriched solute can only be removed from the interface region to the bulk melt through diffusion. Therefore the concentration difference Δc between c_l^e (concentration in the melt at the interface) and c_l (concentration in the bulk melt) is taken as the driving force for solidification. Thermo-dynamic equilibrium at liquid–solid interface exists, therefore c_l^e can be determined from the local temperature T, i.e. $c_l^e = (T - T_f)/m$ according to the phase diagram (Fig. 1). c_l is calculated from the solute conservation equation (3).

In addition to the driving force term Δc, M_{ls} is proportional to the overall solid–liquid interface area. Thus, it depends on the grain density n and the grain surface area πd_s^2 (Eq. (7)). The term f_l is the Avrami-factor. All other factors influencing the solidification rate are gathered in the empirical constant g_α (mm/s). g_α is named here as the 'growth factor'.

2.4. Numerical implementation

The conservation equations (1)–(5) are numerically solved with a control-volume based finite difference method. A CFD software FLUENT version 4.5.6 is used. FLUENT is a trademark of Fluent Inc., USA. Both the liquid and solid share a single pressure field p. The pressure correction equation is obtained from the sum of the normalised mass continuity equations (1) using an extended SIMPLE algorithm [29]. For each time step, up to 60 iterations were necessarily made to decrease the normalised residual of c_l, c_s, f_s, $\vec{u}_l$, $\vec{u}_s$, p and n below the convergence limit 10^{-4}, and h_l and h_s below

10^{-6}. On each iteration the auxiliary quantities d_s and μ_s are updated first. We then calculated the exchange terms U_{ls}, C_{ls} , Q_{ls} and the source term N and M_{ls} based on the last iteration, and finally solved the conservation equations of momentum, mass, enthalpy and species.

The mesh density impacts the calculation accuracy, especially near the wall (sharp gradient) regions. Referring to the boundary-layer theory [30], the mesh adjacent to the wall should obey

$$\Delta\delta \cdot \sqrt{\frac{\rho_l \cdot \vec{u}_l^{\infty}}{\mu_l \cdot \tilde{y}}} \leqslant 1 \tag{15}$$

where $\vec{u}_l^{\infty}$ is the free-stream velocity, $\tilde{y}$ the distance along the wall from the starting point of the boundary layer, $\Delta\delta$ the distance to the wall from the adjacent cell center. Eq. (15) will be used in Section 3 to determine the necessary cell size for adequate resolution of the wall boundary layers.

FLUENT formulation is fully implicit. Theoretically there is no stability criterion that needs to be met in determining Δt. However, the time steps used impact the accuracy, and hence the reliability of the numerical results. Due to the complexity of the coupling, there is no formulation to determine the optimal Δt. It must be determined empirically by test simulations. In the program, however, an automatic Δt controller is integrated. An initial time step (e.g. $\Delta t = 5 \times 10^{-4}$ s) is given. If more than 40 iterations are needed to meet the convergence criterion, the program will reduce Δt. If in less than 20 iterations converge is met, then a larger Δt is used.

3. Problem description

A 2D ingot casting (Fig. 3) is simulated. The calculation domain is meshed into volume elements of 10×10 mm^2. According to Eq. (15), the mesh must be fine enough to ensure the calculation accuracy. With the maximal velocity of 0.03 m/s in the casting and $\tilde{y}$ taken as the height of the casting 0.18 m, $\Delta\delta$ is estimated to be 5.5 mm. It means the mesh size must be less than 11 mm. The finer the mesh size, the smaller the time step Δt necessary to meet the convergence criterion, and hence the higher the calculation cost. In the simulations the automatic time step controller is activated. The calculation starts with $\Delta t = 5 \times 10^{-4}$ s in the initial stage of solidification, while in the later stage it is then automatically adjusted to 2×10^{-3} s. A single run of the simulation takes five days on a SGI Octane R12000 workstation (Silicon Graphics GmbH, Grasbrunn, Germany).

The casting is filled instantaneously and starts to solidify from an initial temperature of 925 K. The mold remains at a constant temperature of 290 K. The heat exchange coefficient H at the casting–mold interface (W1) is 750 W/(m^2 K). The recent model did not consider the free surface which forms at the top. Therefore we applied a special boundary condition (pressure inlet) with constant temperature, constant concentration and constant pressure at the casting top (I1). The side walls of the inlet (W2) are considered to be thermal isolated (Fig. 3). The hot melt from the inlet continuously feeds the solidification shrinkage. A drawback of this boundary condition is that the casting can never solidify completely, and we are currently working to improve this boundary condition.

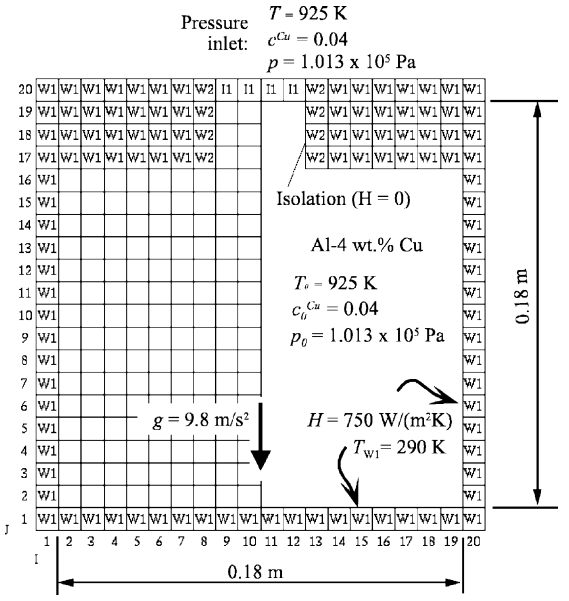

Fig. 3. Diagram of the physical system. The symbols are explained in the text.

Physical properties and phase diagram parameters of this alloy are listed in Table 2. The density of the liquid and solid are constant but different. No thermal solutal convection is considered in the this paper. The parameters used for the nucleation law are $n_{max} = 10^{14}$ m^{-3}, $\Delta T_N = 10$ K, $\Delta T_\sigma = 4$ K. As for the mass transfer rate M_{ls} the grain diameter d_s must be known, an initial grain diameter of $d_s = 1$ μm is assumed. A constant value (5×10^{-4} m/s) for g_α is given.

In order to study the influence of convection and grain movement on globular equiaxed solidification, the following cases are compared.

- *Case I:* Melt convection, grain movement and non-slip condition for the solid phase at the mold interface. All the conservation equations in Table 1 are solved. Grains nucleated in the bulk melt are allowed to move. Grains nucleated on the casting surface adhere to the wall.
- *Case II:* Melt convection and no solid movement. Except for the solid momentum equation, all the other

Table 2
Thermo-physical and thermo-dynamic properties used for the simulation

$\rho_l = 2606\ \mathrm{kg\,m^{-1}}$	$c_{p(l)} = 1179\ \mathrm{J\,kg^{-1}\,K^{-1}}$	$\mu_l = 1.3 \times 10^{-2}\ \mathrm{kg\,m^{-1}\,s^{-1}}$
$\rho_s = 2743\ \mathrm{kg\,m^{-1}}$	$c_{p(s)} = 766\ \mathrm{J\,kg^{-1}\,K^{-1}}$	$T_f = 933.5\ \mathrm{K}$
$k_l = 77\ \mathrm{W\,m^{-1}\,K^{-1}}$	$D_l^{Cu} = 5 \times 10^{-9}\ \mathrm{m^2\,s^{-1}}$	$k = 0.145$
$k_s = 153\ \mathrm{W\,m^{-1}\,K^{-1}}$	$D_s^{Cu} = 8 \times 10^{-13}\ \mathrm{m^2\,s^{-1}}$	$m = -344\ \mathrm{K}$

conservation equations in Table 1 are solved. Grains are not allowed to move, no matter whether they nucleate on the wall or in the bulk melt.

- *Case III:* Melt convection, grain movement and slip condition for the solid phase at the mold walls. This case is same as *Case I*, except for a slip boundary condition applying to the solid phase momentum equation. Grains, no matter whether they nucleate on the wall or in the bulk melt, are allowed to move.

4. Results and discussion

4.1. Case I

This case considers both melt convection and grain movement. A non-slip boundary condition is applied for the solid phase. Simulation results 40 and 80 s after cooling starts are shown in Figs. 4 and 5. Both gray scale and isolines are used to show the distribution of T, f_s, c_{mix}, n and d_s. Each quantity is equally scaled with 30 gray levels, with dark areas representing the highest and bright areas the lowest values. The corresponding value for each isoline is given. The result of c_{mix} and d_s (Fig. 4d) show some enclosed regions, which are marked with a number followed by "+" or "−" implying that the quantity in the enclosed region is larger than (+) or smaller than (−) the values given. $\vec{u}_l$ and $\vec{u}_s$ are shown together with f_s. The arrows of both velocities are continuously scaled starting from zero to a maximum given below each figure.

4.1.1. Solidification sequence

The start of cooling immediately establishes a symmetrical and positive temperature gradient towards the casting center. As soon as T drops below the liquidus

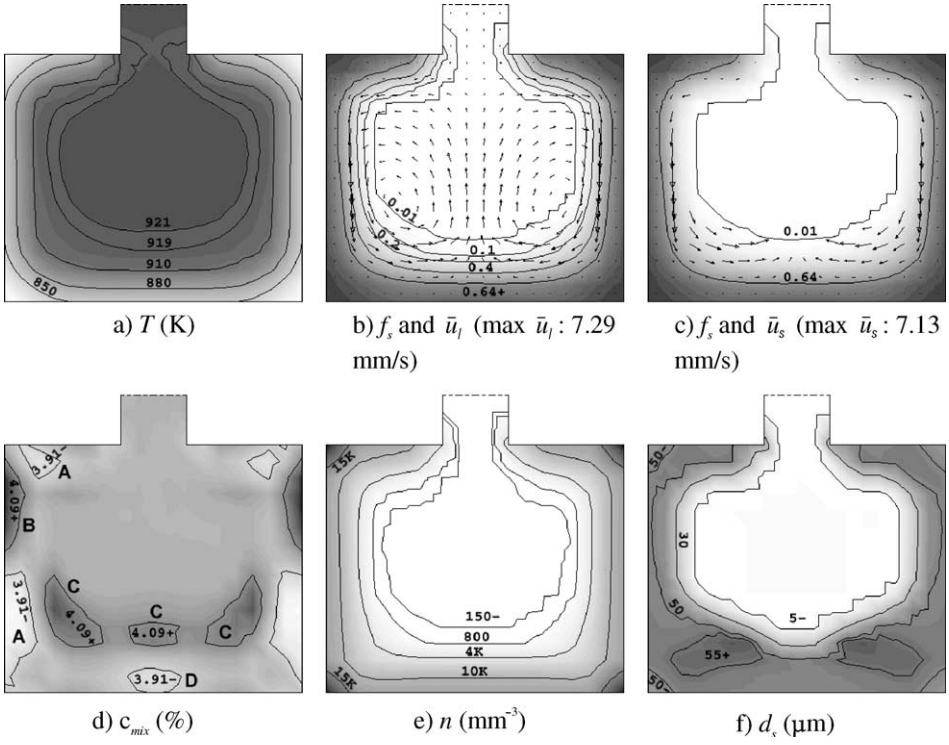

Fig. 4. Simulation results of *Case I*, 40 s after the cooling starts. The arrows of both velocities are linearly scaled starting from zero to the maximum value given. All other quantities are shown with isolines together with different gray levels, with dark areas showing the highest value and bright areas the lowest.

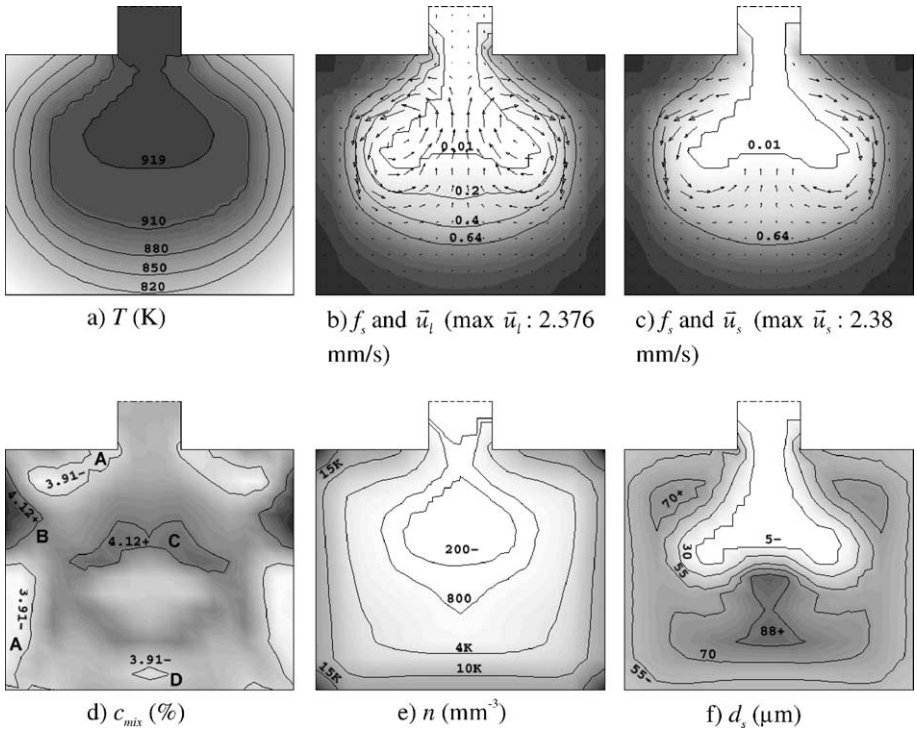

a) T (K) b) f_s and $\vec{u}_l$ (max $\vec{u}_l$: 2.376 mm/s) c) f_s and $\vec{u}_s$ (max $\vec{u}_s$: 2.38 mm/s)

d) c_{mix} (%) e) n (mm^{-3}) f) d_s (μm)

Fig. 5. Simulation results of *Case I*, 80 s after the cooling starts. The arrows of both velocities are linearly scaled starting from zero to the maximum value given. All other quantities are shown with isolines together with different gray levels, with dark areas showing the highest value and bright areas the lowest.

temperature, the melt is undercooled, i.e. $\Delta T \equiv T_f + mc_l - T > 0$ and nucleation ($N > 0$) and solidification ($M_{ls} > 0$) begin. This occurs first in the corners, then along the mold walls, and finally in the bulk melt.

In the initial stage the grains nucleating at the corners and along the walls do not move. They are modeled to adhere to the mold wall by applying a non-slip boundary condition to the solid momentum equation. As solidification starts, solidification shrinkage ($\rho_l > \rho_s$) leads to a feeding flow, the details of which are discussed in Section 4.2 *Case II*. A significant feature at the initial stage is that the isotherm and the f_s isolines are almost identical and very symmetrical, and that they move gradually from corners and casting surface regions towards the casting center, showing that the solidification process is initially controlled by heat extraction only.

As solidification proceeds, grains nucleating near the casting surface and without direct contact with the mold wall sink along the vertical wall (Fig. 4c). The solid and liquid are coupled through the momentum exchange terms, and therefore the sinking grains drag the surrounding melt. As a result, the melt at the bottom region moves inwards and then rises up, providing space for the oncoming grains and melt. Hence, two vortices form in the melt (Fig. 4b). Vice versa, the vortices have a strong impact on the velocity field of the grains. The movement of the grains increases the fraction solid f_s in the lower regions, quickly exceeding the packing limit and stopping grain movement. This phenomenon is known as grain settlement or sedimentation. Grain movement and sedimentation influence the solidification sequence. The f_s isolines in the lower corners proceed faster than in the upper corners (Fig. 5b and c), and in the lower corners faster than in the side wall regions.

The melt current has a strong impact on the velocity field of the grains, and the grains nucleated near the upper boundary regions do not sink directly, but move towards (or diverge to) the upper corners (Figs. 4c and 5c). The only explanation for this is the impact of the melt current. Predictably, grains also settle near the upper corner regions facing the oncoming grains.

The low part of the f_s isoline (0.01) also protrudes towards the hot center (Fig. 5c). The melt currents (vortices) transport the grains from lateral or bottom regions to the hot center, where remelting ($M_{ls} < 0$) occurs. More details of the remelting was presented in a previous paper [19].

4.1.2. Macrosegregation formation

Segregation phenomenon is understood to be caused by solute partitioning at the solidification interface. If a control volume is isolated from its neighboring volume

and there is no convectional and diffusional mass exchange, the solute partitioning can only cause microsegregation, but no macrosegregation would occur. Here grain movement and melt convection are present. Thus, there is mass exchange among neighboring control volumes through grain movement and melt convection. In fact a complicated macrosegregation pattern is predicted in Figs. 4d and 5d. The macrosegregation is quantitatively expressed with a mixture concentration c_{mix}. The different segregation regions are marked with A–D. The regions with c_{mix} lower than the average concentration (4%) have negative segregation such as A and D, the regions with c_{mix} higher than 4% have positive segregation such as B and C.

The negative segregation A in the upper corner region is caused by grain movement and feeding flow. Referring to Fig. 4b the 0.64 f_s-isoline (approximately the packing limit) is not symmetrical in the upper corner. The part of the 0.64 f_s-isoline located near the negative segregation zone A proceeds faster (or the packed region becomes wider) than the corresponding part of positive segregation zone B. This non-symmetry of the solidification sequence in the upper corner is caused by grain movement and settlement. The velocity field of the moving solid shows that the grains nucleated near the upper boundary regions tend to move towards the corner, whereas those nucleated near the side wall just below the upper corner sink to the bottom. The grains moving towards the corner cause the local f_s to increase. As the f_s exceeds the packing limit, the solid velocity vanishes and the oncoming grains adhere and settle there. According to Eq. (11), c_{mix} is determined by f_s, f_l, c_l and c_s. c_s is much lower than c_l. Thus, regions with a higher grain settlement rate has a lower c_{mix}. This is the reason why the negative segregation A in upper corner forms. In addition to the appearance of the negative segregation zone A, in the course of solidification this zone shifts slowly downwards. As the f_s isolines proceed, and the oncoming grains continue to settle and produce new negative segregation, while the melt penetrates through the voids between the packed grains to feed solidification shrinkage. The solute-enriched feeding melt can partially offset the existing negative segregation near the casting wall so that the negative segregation there weakens. As a consequence the negative segregation zone A shifts (not moves) from the wall into the casting.

The positive segregation area B just below the upper corner is also caused by grain movement and feeding flow. As the packing limit is exceeded, the grains at the upper corner cannot move. However, just below the corner when the local fraction solid is still below the packing limit, the grains can sink. From this area grains leave the region B. The volume of the exiting grains must be filled by melt. However, the available melt is rich in solute. The direct outcome of this phase transport phenomenon, i.e. the exit of the solute-deficient solid and the entry of the solute-enriched melt, is the increase of the local mixture concentration c_{mix}. A second reason for the positive segregation area B is the feeding flow. As the local fraction solid exceeds the packing limit, the feeding melt will strengthen the positive segregation.

The negative segregation zone A near the lower corner forms by means of the same mechanisms as in the upper corner, i.e. grain sedimentation and feeding flow. As grain settlement rate is much higher here, this negative segregation is stronger than that at the upper corners.

The positive segregation zone C just close to A at the lower corner (Fig. 4d) is caused by melt flow. As the grains settle into zone A, solute-enriched melt has to leave this region so as to provide space for the settling grains. This solute-enriched melt is brought out of region A by the convection current, and the positive segregation zone C is just near to it. This positive segregation forms temporarily in the bulk melt. It is not stationary and will thus move with the melt flow while solidification proceeds.

The negative segregation region D is also caused by sedimentation. The solute-deficient grains are brought by the convection current from the left and right to meet in the central bottom region where they sink and settle. The solid velocity vanishes as the local fraction solid exceeds the packing limit. The settling grains in this region pile up, and so form the negative segregation D.

Liquid convection contributes to the central positive segregation C (Fig. 5d). As the negative segregation region D forms, the convection currents bring the solute-enriched liquid out of that region to form a positive segregation C just above the region D (Fig. 4d). This segregation is also formed in the bulk melt. As solidification proceeds, it moves gradually towards the last region to solidify. In fact, in the late stage of solidification, all positive segregated regions C move to the last region to solidify to produce a large positive segregated central area (Fig. 5d).

4.1.3. Grain evolution

Grain formation comprises two key processes: nucleation and grain growth. Three interdependent parameters are used to quantitatively describe the processes: grain density n, fraction solid f_s and grain diameter d_s. f_s is obtained by solving the mass conservation equation (1), n by solving the grain transport equation (5), and d_s is determined by Eq. (12).

We implement an empirical heterogeneous nucleation law [23,25,28] in the grain transport equation as the source term. According to this law, the undercooling $\Delta T = T_f + m \cdot c_l - T$ is the only driving force for the nucleation (Fig. 2). The high grain density n at the corner and in the surface region, predicted in this simulation (Figs. 4e and 5e), actually arises from the high

nucleation rate N, namely the high ΔT. The ΔT achieved in the surface region and at the corner is 6–8 K, which is much higher than the maximum ΔT achieved in the bulk melt region (<1 K). As discussed in 4.1.2, grain movement is negligible in the initial stage of cooling, especially at the corner and casting surface regions. Therefore, the grain density there will remain unchanged in the course of solidification.

The distribution patterns of f_s and n differ, especially in late stage of solidification (Fig. 5). Eqs. (1) and (5) show that both the solid phase $\rho_s \cdot f_s$ and the grain density n are transported according to the same velocity field $\vec{u}_s$. If only the transport phenomena were considered (without nucleation and without solidification), the distribution patterns of both f_s and n should be similar. In fact transport is not the only factor influencing the f_s and n. The n changes according to grain movement and nucleation rate. f_s is the outcome of the solid phase transport and solidification. The nucleation rate is based on Eq. (6) and the solidification rate is defined by Eq. (7). Therefore, the distribution patterns of f_s and n are not necessarily equal.

n is different in the corners and surface regions. However, the grain size d_s appears to be relatively uniform. The maximum grain density n in the corners is predicted to be about 2×10^{-4} mm^{-1}, and along the casting surface 1.0–1.5 $\times 10^{-4}$ mm^{-3}. The grain size d_s is about 50–55 μm in the corner and surface regions. The main reason for this is that during the initial stage of solidification the high grain density regions correspond to high fraction solid regions. According to Eq. (12), d_s is proportional to $\sqrt[3]{f_s/n}$.

Two symmetrical large grain zones appear near the lower corners (Fig. 4). The solid velocity field indicates that the large grains may have been transported from the region of the vertical wall, where the grains nucleate, sink and grow. As they reach the lower corner regions, they have become relatively large. As solidification proceeds both large grain zones seem to move inwards and join to form a central zone of large grains. The grains continue to grow while moving. Since our model applies an open thermal isolated boundary condition at the casting top, the casting can never solidify completely.

According to the nucleation model, grain destruction (or dissolution) is allowed for grains exposed to overheating (negative undercooling) and for a local fraction solid less than 10^{-4}. Our simulation shows the remelting phenomena near the hot center. However, there is no grain destruction as the local f_s is larger than 10^{-4}.

4.2. Case II

Grain movement is explicitly excluded in *Case II*. The solid phase is assumed to be rigid and to adhere to the mold walls. The grains start to nucleate at and grow from the corners and the mold walls. Then they grow towards the casting center. The melt continuously feeds solidification shrinkage. The solidification morphology is still assumed to be globular equiaxed, and Eq. (6) is still applied for nucleation and Eq. (7) for mass transfer. Fig. 6 (left) shows the solidification sequence, feeding phenomenon and macrosegregation formation to be similar to the columnar solidification. Fig. 6 (left) shows the results of T, f_s, $\vec{u}_l$ and c_{mix} 40 s after start of cooling, directly compared to *Case I* (right).

Although not so significant, there are differences in the isotherm between the *Cases II* and *I* (Fig. 6a). The 921 K isotherm of *Case II* is slightly lower than that of *Case I*. The reason for this is the grain sedimentation in *Case I*: grains move along the side wall downwards, settle at the bottom regions, causing the hot center to move upwards. The same statement applies to the f_s isolines (Fig. 6b). Without grain movement the f_s isolines proceed at a similar speed from the bottom and the side walls. The dominant factor governing the solidification sequence if there is no grain movement is heat extraction through the mold wall. The heat extraction rates through the bottom and side walls are equal.

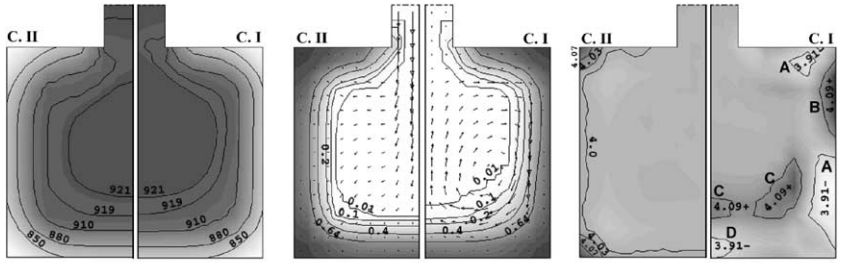

a) T (K) b) f_s and $\vec{u}_l$ (max $\vec{u}_l$: 7.29 for *Case I*; 0.3 mm/s for *Case II*) c) c_{mix} (%)

Fig. 6. Simulation results of *Case II* (left), compared to *Case I* (right), 40 s after start of cooling. The arrows of the velocity are linearly scaled starting from zero to the maximum value given. All other quantities are shown with isolines together with different gray levels, with dark areas representing the highest value and bright areas the lowest.

The flow patterns of *Cases I* and *II* are completely different (Fig. 6b). Without grain movement only feeding flow is present (thermo-solutal convection is not considered in this paper). The melt flows through the inlet, and distributes uniformly and symmetrically through the mushy zone to feed solidification shrinkage. In the presence of grain movement, both feeding flow and flow due to grain movement occur. The grain movement causes vortices in the melt. If there is no grain movement, the maximum $\vec{u}_l$ is 0.3 mm/s appearing at the inlet. However, the maximum $\vec{u}_l$ in the case of grain movement is 7.2 mm/s near the side walls, where grain sinking velocity is at its maximum, indicating that flow due to grain movement is much stronger than the feeding flow. Obviously feeding flow is similar in both cases. However, in *Case I* the arrows of the feeding flow at the inlet are 24 times smaller than those of *Case II*. Thus the arrows at the inlet cannot be seen in *Case I*.

In the absence of grain movement, positive segregations are predicted in the corner regions (Fig. 6c), but these are less complicated and less serious than in *Case I*. The solidification rate at the corner is higher than all other regions. The melt penetrates the voids between the grains to feed solidification shrinkage. As discussed above the solute-enriched feeding melt increases the c_{mix} locally.

4.3. Case III

In contrast to *Case I*, *Case III* applies a slip boundary condition for the momentum equation of the solid phase. Thus, the grains are free to move no matter whether they nucleate on the wall or in the bulk melt. The boundary condition plays a very important role in solidification and the formation of structure [3]. In real casting practice, both slip and non-slip walls may present. The comparison of the two extreme cases helps to understand the influence of the boundary condition on the solidification process. The simulation results of *Cases III* and *I* are compared in Fig. 7.

With the slip boundary condition the grains are free to sink as soon as they nucleate on the wall, while with the non-slip condition the grains on the casting surface do not move. Therefore, grain movement in *Case III* is much stronger than in *Case I* (Fig. 7). The maximum solid velocity in *Case III* at 40 s is 9.75 mm/s, while in *Case I* 7.13 mm/s. A direct outcome of the strong grain movement in *Case III* is the high grain sedimentation rate in the bottom region. In *Case III* the f_s isolines in the bottom regions are faster than in *Case I*. As melt flow and solid movement are coupled, the strong grain movement produces the strong melt flow current. In turn the strong flow current influences grain movement. The consequence is that the hot center moves upwards

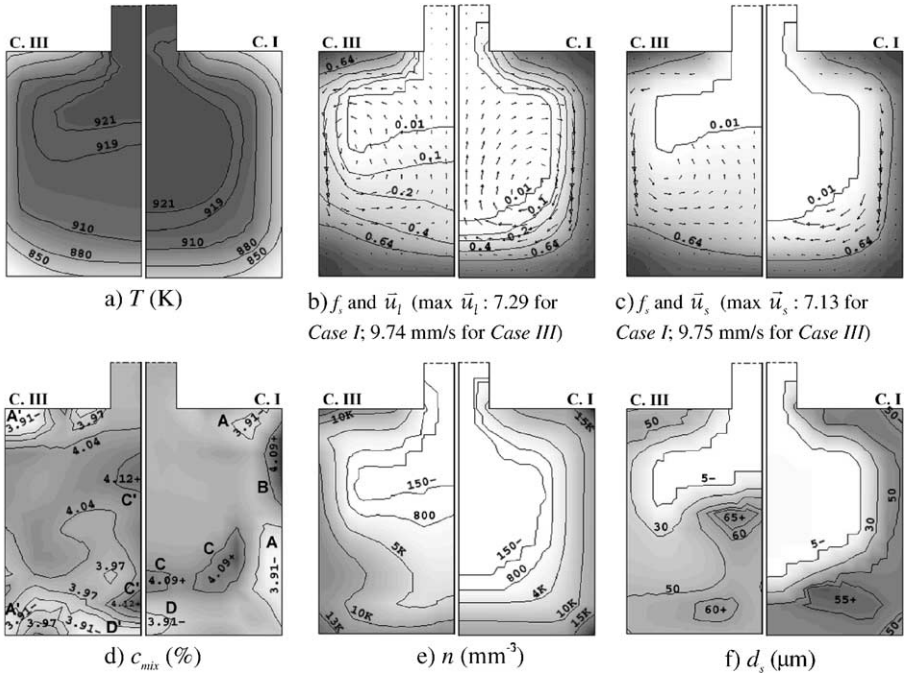

Fig. 7. Simulation results of *Case III* (left), compared to *Case I* (right), 40 s after the start of cooling. The arrows of both velocities are linearly scaled starting from zero to the maximum value given. All other quantities are shown with isolines together with different gray levels, with dark areas representing the highest value and bright areas the lowest.

significantly, as the isotherms and the f_s isolines show (Fig. 7a and b).

In *Case III* the grains in the upper corner are allowed to sink. However, due to the high cooling rate, especially in the initial stage, the solidification rate is so high that the f_s exceeds the packing limit before the grains have time to move out of this region. While cooling continues, the front line of the packed solid region ($f_s = 0.64$) proceeds. The corner is now rigid and nearly solid, and can move downwards, if the gap appearing between the rigid solid corner and the mold can be refilled with melt. This is not possible instantaneously. In reality plastic deformation in the porous medium would continuously open a corresponding gap from the edge of the rigid solid phase towards the corner. As our simulation does not consider plastic deformation in the solid phase, a gap does not form and the rigid, almost solid phase remains in the corner. As already discussed in Section 4.1.1, grains nucleated near the upper boundary regions do not sink directly, but move towards (or diverge to) the corner due to the melt flow present. Grains also settle near the upper corner region facing the oncoming grains (Fig. 7c).

The segregation pattern of *Case III* appears to differ from that of *Case I* (Fig. 7d). The negative segregation zone in the upper corner, marked with A′, is caused by grain sedimentation. The grains nucleating near the upper boundary also move towards (or diverge to) the corner and settle there, producing negative segregation. The settling grains squeeze the segregated melt out of the region. Generally corresponding to the negative segregation zone A′, there must be a positive segregation zone B′ which forms just below. Due to the slip boundary condition, the melt flow is so strong that the segregated melt is immediately transported elsewhere. Just below the corner f_s is about 0.4, which is much lower than the packing limit (Fig. 7b).

Zone D′ is caused by sedimentation, similar to zone D in *Case I*. Zone A′ in the lower corner region is also caused by sedimentation. Because of the slip boundary condition, the sedimentation zone in the lower corner region becomes lower and wider. Therefore, the negative segregation zone A′ becomes wider and lower. As solidification proceeds, both zone A′ and D′ join together (25 s after the start of cooling).

As discussed in Section 4.1.2, there must be a positive segregation zone C′ corresponding to each negative segregation zone A′ or D′ in the bottom regions. The segregated melts are squeezed out of the settling zones and form three separate positive segregation C′ just near or above the negative segregation zones. However, due to the strong flow current in *Case III* the two positive segregation zones C′ formed near the lower corners move inwards quickly, and join to form a central positive segregation zone C′ (15 s after the start of cooling). As a consequence of the strong flow and the complexity of the flow pattern, the central positive segregation C′ is broken into two separate zones: one located in the hot center and one near the lower central region (Fig. 7d).

Grain density n distribution in *Cases III* and *I* are different (Fig. 7e). n near the corner in *Case III* is 1.0–1.3×10^4 mm^{-3}, while in *Case I* it is 1.5×10^4 mm^{-3} . In *Case III* n in the central part is significantly higher. The reason is again the strong grain movement resulting from the slip boundary condition. This also produces the grain density n in the upper corners (1.0×10^4), which is different from n in the lower corners (1.3×10^4), because grains sink from the upper corner and settle in the lower corner. In *Case I* there is no difference in n between the upper and lower corners.

The larger grains in the central regions are actually transported from other regions, with the same mechanism as what described in Section 4.1. The grains nucleate and sink along the vertical wall. In the meantime they grow. As they reach the lower regions, they have become relatively large. As solidification proceeds, both large grain zones move from the left and right with the solid velocity inwards and join to form a large central grain zone.

4.4. Accuracy and reliability analysis

As mentioned in Section 2.4, the mesh density and time step influence the calculation accuracy. Fine mesh and small time step improve the accuracy, but increase the calculation cost. In this paper, the mesh size is determined according to the boundary theorem [30]. The mesh size in the large gradient region (the wall boundary) is smaller than the one estimated from the criterion Eq. (15). This mesh criterion ensures that velocity gradient at the wall is adequately approximated by the difference expression. In order to reduce the calculation cost, the sophisticated computational techniques, e.g. unstructured meshes for the critical regions with sharp gradient of the variables and parallel computing, can be used.

An ideal boundary condition at the casting top, i.e. pressure inlet, is applied. Hot melt flows through this inlet to feed the casting continuously. A drawback of this boundary condition is that the casting can never completely solidify. Therefore, in future work it is necessary to model the free surface boundary which forms at the casting top, including the concentrated cavities in the casting center due to the solidification shrinkage.

Only sedimentation induced flow and feeding flow are considered here. The thermo-solutal convection would also influence the flow pattern and, consequently, the macrosegregation distribution. An other limitation of the recent two-phase model is the laminar flow. The authors have previously discussed the validation of the laminar model for the problem described in Fig. 3 [19]. If the system Reynolds number ($D \cdot \vec{u}_l \cdot \rho_l / \mu_l$) exceeds

the criterion number 2100 [26], the turbulence model must be considered.

The micromodels, which are used to describe the nucleation, the grain growth kinetics, the interphase heat and mass exchanges, and the interaction between the phases such as drag force, are coupled into the macro-conservation equations. The validity of the micromodels are studied previously [19–21,23,26–28], not repeated here. However, the authors are of the opinion that further parameter studies are necessary, even alternative models would be developed in consideration of some special solidification processes, growth morphology and alloys.

Despite the model complexity and some model assumptions, evaluation efforts in another study [31] with the same two-phase model and on the same alloy (Al–4 wt.% Cu) but different casting geometry configuration (plate casting) were made by comparing the numerical prediction with the experiment. The numerically predicted grain size distribution was found to agree reasonably with experimental result, and the EDX analyzed macrosegregation showed the same tendency as the simulation.

5. Conclusions

Solidification in an aluminum (Al–4 wt.% Cu) ingot casting including nucleation, grain evolution, grain movement, sedimentation, melt convection, solute transport and macrosegregation was simulated with a two-phase volume averaging approach. To investigate the influence of grain movement and melt convection on the solidification, we studied three extreme cases with different model assumptions. The following conclusions were made.

- Grain movement and sedimentation influence the solidification sequence (the process of the fraction solid isoline). Where solid movement does not exist (analogous to the pure columnar growth), the solidification sequence and the isotherms proceed equally from the bottom and side walls. Where the grain movement is present, sedimentation in the bottom regions causes the solidification sequence and the isotherms to proceed faster in the bottom regions than in the side wall regions.
- The flow patterns with and without grain movement are obviously different. If there is no grain movement, feeding flow is symmetrical. In the event of grain movement the grains sinking along the mold wall induce vortices, which in turn influence solid movement and bring grains to the bulk melt.
- Grain settlement is responsible for the negative segregation in globular equiaxed solidification. In *Cases I* and *III*, settlement was found (i) near upper corners; (ii) near lower corners; and (iii) in the middle bottom region, where negative segregations occur.
- There are two reasons for positive macrosegregation: (i) feed of segregated melt to packed zones and (ii) squeezing out of segregated melt by settling grains. Areas of positive segregation caused by the latter may not be stationary and thus move during solidification with the melt flow. Those caused by the former do not move.
- Grain movement and convection influence the grain size distribution. In *Case III* with slip boundary condition for the solid phase, grains are free to move everywhere. Some grains sink from the upper corners towards the lower corners, some move to the casting center following the strong melt flow, hence raising the grain density in the lower corners and the central regions.
- The large grains in the central area in *Cases I* and *III* are transported from other regions. Some grains nucleate near the wall, sink, and move inwards or then towards the casting center. The grains continue to grow while moving.

Acknowledgements

This work is financially supported by the German Science Foundation (DFG) as part of the collaborative research centers SFB 370 and SFB 289. The authors also acknowledge the technical assistance of Dr. Pelzer and Dr. Braun, Fluent Deutschland GmbH, Darmstadt, Germany.

References

[1] M.C. Flemings, Solidification Processing, McGraw-Hill, New York, 1974.
[2] J. Campbell, Castings, Butterworth-Heinemann Ltd., Oxford, 1991.
[3] A. Ohno, Solidification: The Separation Theory and its Practical Applications, Springer-Verlag, Berlin, 1987.
[4] W.D. Bennon, F.P. Incropera, A continuum model for momentum, heat and species transport in binary solid–liquid phase change systems—I: Model formulation, Int. J. Heat Mass Transfer 30 (1987) 2161–2170.
[5] V.R. Voller, C. Prakash, A fixed grid numerical modeling methodology for convection–diffusion mushy region phase-change problems, Int. J. Heat Mass Transfer 30 (1987) 1709–1719.
[6] Q.Z. Diao, H.L. Tsai, Modeling of the formation of under-riser macro-segregation during solidification of binary alloys, Metall. Mater. Trans. A 25 (5) (1994) 1051–1064.
[7] J. Ni, F.P. Incropera, Extension of the continuum model for transport phenomena occurring during metal alloy solidification—I: The conservation equations, Int. J. Heat Mass Transfer 38 (1995) 1271–1284.
[8] J. Ni, F.P. Incropera, Extension of the continuum model for transport phenomena occurring during metal alloy

solidification—II: Microscopic considerations, Int. J. Heat Mass Transfer 38 (1995) 1285–1296.
[9] C.J. Vreeman, M.J.M. Krane, F.P. Incropera, The effect of free-floating dendrites and convection on macro-segregation in direct cast aluminum alloys—I: Model development, Int. J. Heat Mass Transfer 43 (2000) 677–686.
[10] C.J. Vreeman, F.P. Incropera, The effect of free-floating dendrites and convection on macro-segregation in direct cast aluminum alloys—II: Predictions for Al–Cu and Al–Mg alloys, Int. J. Heat Mass Transfer 43 (2000) 697–704.
[11] H.J. Thevik, A. Mo, T. Rusten, A mathematical model for surface segregation in aluminum direct chill casting, Metall. Mater. Trans. B 30 (1999) 135–142.
[12] C. Beckermann, R. Viskanta, Mathematical modeling of transport phenomena during alloy solidification, Appl. Mech. Rev. 46 (1993) 1–27.
[13] J. Ni, C. Beckermann, A volume-averaged two-phase model for transport phenomena during solidification, Metall. Trans. B 22 (1991) 349–361.
[14] C.Y. Wang, C. Beckermann, Equiaxed dendritic solidification with convection—I: Multiscale-multiphase modeling, Metall. Mater. Trans. A 27 (1996) 2754–2764.
[15] C.Y. Wang, C. Beckermann, Equiaxed dendritic solidification with convection—II: Numerical simulation for an Al–4 wt% Cu alloy, Metall. Mater. Trans. A 27 (1996) 2765–2783.
[16] C.Y. Wang, C. Beckermann, Equiaxed dendritic solidification with convection—III: Comparisons with NH_4Cl–H_2O experiments, Metall. Mater. Trans. A 27 (1996) 2784–2795.
[17] C. Beckermann, Modeling segregation and grain structure development in equiaxed solidification with convection, JOM 49 (1997) 13–17.
[18] A.V. Reddy, C. Beckermann, Modeling of macrosegregation due to thermosolutal convection and contraction-driven flow in direct chill continuous casting of an Al–Cu round ingot, Metall. Mater. Trans. B 28 (1997) 479–489.
[19] A. Ludwig, M. Wu, Modeling of globular equiaxed solidification with a two-phase approach, Metall. Mater. Trans. A 33 (2002) 3673–3683.
[20] A. Ludwig, G. Ehlen, M. Pelzer, P.R. Sahm, Simulation of solid movement during solidification by a simple multi-phase approach, in: P.R. Sahm et al. (Eds.), Proceeding of CWASP IX, SIM2000, Aachen, Shaker-Verlag, 2000, pp. 175–182.
[21] A. Ludwig, M. Wu, G. Ehlen, P.R. Sahm, Numerical description of solid movement during equiaxed solidification using a two-phase modeling approach, Materials Week 2000, September 25–28, 2000, Munich, Germany.
[22] Ø. Nielsen, B. Appolaire, H. Combeau, A. Mo, Measurements and modeling of the microstructural morphology during equiaxed solidification of Al–Cu alloys, Metal. Mater. Trans. A 32 (2001) 2049–2060.
[23] M. Rappaz, Modeling of microstructure formation in solidification processes, Int. Mater. Rev. 34 (1989) 93–123.
[24] W. Kurz, D.J. Fisher, Fundamentals of Solidification, Trans Tech Publications, Aedemannsdorf, Switzerland, 1989.
[25] P. Thevoz, J.L. Desbiolles, M. Rappaz, Modeling of equiaxed microstructure formation in casting, Metall. Trans. A 20 (1989) 311–322.
[26] R.B. Bird, W.E. Stewart, E.N. Lightfoot, Transport Phenomena, John Wiley & Sons, New York, NY, 1960.
[27] C.Y. Wang, S. Ahuja, C. Beckermann, H.C. de Groh, Multiparticle interfacial drag in equiaxed solidification, Metall. Mater. Trans. B 26 (1995) 111–119.
[28] W. Oldfield, Trans. ASM 59 (1966) 945–961.
[29] S.V. Patankar, Numerical Heat Transfer and Fluid Flow, Hemisphere Publishing Corp., Washington, DC, 1980.
[30] H. Schlichting, Boundary-layer Theory, McGraw-Hill Publishing Co., New York, NY, 1979.
[31] M. Wu, A. Ludwig, Influence of phase-transport phenomena on macrosegregation and structure formation during solidification, Adv. Eng. Mater. 5 (2003) 62–66.